

Spatial control of laser-induced doping profiles in graphene on hexagonal boron nitride

Christoph Neumann,^{†,‡} Leo Rizzi,[†] Sven Reichardt,^{†,¶} Bernat Terrés,^{†,‡} Timofiy
Khodkov,^{†,‡} Kenji Watanabe,[§] Takashi Taniguchi,[§] Bernd Beschoten,[†] and
Christoph Stampfer^{*,†,‡}

*JARA-FIT and 2nd Institute of Physics, RWTH Aachen University, 52074 Aachen, Germany, Peter
Grünberg Institute (PGI-9), Forschungszentrum Jülich, 52425 Jülich, Germany, Physics and
Materials Science Research Unit, Université du Luxembourg, 1511 Luxembourg, Luxembourg,
and National Institute for Materials Science, 1-1 Namiki, Tsukuba, 305-0044, Japan*

E-mail: stampfer@physik.rwth-aachen.de

KEYWORDS: Graphene, p-n junction, electric transport, boron nitride, photo-induced doping,
laser

Abstract

We present a method to create and erase spatially resolved doping profiles in graphene-hexagonal boron nitride (hBN) heterostructures. The technique is based on photo-induced doping by a focused laser and does neither require masks nor photo resists. This makes our technique interesting for rapid prototyping of unconventional electronic device schemes, where the spatial resolution of the rewritable, long-term stable doping profiles is only limited by the

*To whom correspondence should be addressed

[†]JARA-FIT and 2nd Institute of Physics, RWTH Aachen University, 52074 Aachen, Germany

[‡]Peter Grünberg Institute (PGI-9), Forschungszentrum Jülich, 52425 Jülich, Germany

[¶]Physics and Materials Science Research Unit, Université du Luxembourg, 1511 Luxembourg, Luxembourg

[§]National Institute for Materials Science, 1-1 Namiki, Tsukuba, 305-0044, Japan

laser spot size (≈ 600 nm) and the accuracy of sample positioning. Our optical doping method offers a way to implement and to test different, complex doping patterns in one and the very same graphene device, which is not achievable with conventional gating techniques.

In recent years, the stacking of two-dimensional materials bound by van der Waals interaction has emerged as an interesting approach for designing and studying novel device concepts for electronic¹⁻⁴ and optoelectronic applications.⁵⁻⁷ In particular, material stacks built around graphene (Gr) promise interesting electronic properties⁸⁻¹² and many possibilities for hosting high-quality devices. Different two-dimensional materials have been shown to be favorable substrates for graphene in such stacks.¹³ Most prominently, hexagonal boron nitride (hBN) has been used in numerous studies to encapsulate graphene and enable high-quality graphene devices.^{11,14-17} In order to enable functional electronic devices, local gates are usually used to implement p-n junctions or other doping profiles. Recently, an alternative way has been reported for changing the charge carrier doping in hBN-Gr stacks by optical illumination.¹⁸ Notably this photo-induced doping in heterostructures of graphene and hBN¹⁸ is significantly more efficient than for graphene on SiO₂.^{19,20} Here we show that a focused laser can be used to create charge doping patterns, such as lateral p-n junctions, with high spatial precision and long lifetimes in Gr-hBN heterostructures. Importantly the presented laser-induced doping technique works completely without masks and photo-resists. We show that the lateral resolution is essentially only limited by the laser spot size and accuracy of sample positioning. The process maintains the high electronic mobility of the graphene sample and offers distinct advantages over conventional gate electrodes, such as rewritability, the possibility of changing and controlling doping profiles in a single device, and a reduction of process steps. This makes our findings highly interesting for prototyping unconventional electronic device schemes based on graphene.

Our sample consists of a single-layer graphene sheet which is encapsulated by two multi-layer hBN flakes. This material stack is obtained by a dry and resist-free transfer process, which has been shown to result in high-mobility graphene devices.^{9,10,21} The resulting heterostructure is placed on a highly doped silicon substrate with a 285 nm thick SiO₂ layer (Figure 1a). The sample

is structured into a Hall bar using electron beam lithography and reactive ion etching. Finally, it is contacted via chrome/gold electrodes on the sides of the heterostructure.⁹ The width of the Hall bar is 1.9 μm and the total length is 12.3 μm . For transport measurements, we use a four-probe geometry with a constant source-drain current of 50 nA (Figure 1b). The longitudinal voltage V_{xx} is probed at the two lower contacts. Our optical setup consists of a confocal laser system with a 100 \times objective. For excitation, we use a laser with energy $E_L = 2.33$ eV and an intensity between 2 and 4 mW. Reflected and scattered light is detected via a single mode optical fiber and a spectrometer with a 1200 lines/mm grating. The setup enables us to locally investigate the Raman signal of the sample at 4.2 K. A typical Raman spectrum obtained on the Hall bar is presented in Figure 1c. The characteristic graphene Raman G line (around 1580 cm^{-1}) and the 2D line (around 2680 cm^{-1}) are observed as well as a line at around 1365 cm^{-1} , which originates from E_{2g} phonons in the hBN layers. In particular, the small full width at half maximum (FWHM) of the graphene 2D line of around 17 cm^{-1} is an indication of the high crystal quality and local flatness of the encapsulated graphene sheet.^{12,22}

A scanning force microscopy (SFM) image of the Hall bar is shown in Figure 1e. Comparison with a scanning Raman microscopy image (Figure 1f), showing the intensity of the prominent Si Raman line at 520 cm^{-1} (see spectra in Figure 1d), reveals the high spatial resolution of our optical setup. The silicon peak intensity is reduced when the substrate is covered by the hBN-Gr heterostructure (compare the red and black curves in Figure 1d) and is completely suppressed in metal-coated areas (i.e. on the gold electrodes). Imaging the Si peak intensity allows us to precisely navigate across the device, which is needed for the subsequent experiments. By comparing line cuts of the SFM and scanning Raman microscopy images across the Hall bar (compare Figures 1g and 1h), we can further gain a quantitative measure for the laser spot size. Assuming a Gaussian laser profile and convoluting it with a step function, we adjust the width of the Gaussian so that the convoluted profile matches the Raman line cut (see Figure 1h). This way, we estimate the standard deviation of the Gaussian to be around 250 nm (green curve in Figure 1h), which corresponds to a FWHM of ~ 590 nm. This value sets the size of our laser spot and limits the spatial resolution of

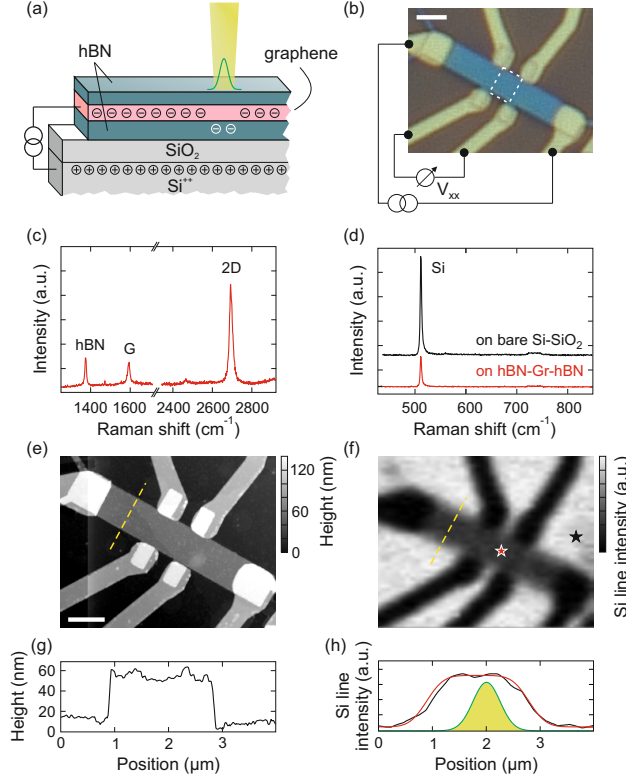


Figure 1: (a) Schematic illustration of an hBN-Gr-hBN sandwich on a $\text{Si}^{++}/\text{SiO}_2$ substrate. The sample can be locally illuminated by a laser ($E_L = 2.33$ eV). In the illuminated area, the hBN is charged screening away the electric field of the back gate. (b) Optical image of an hBN-Gr-hBN Hall bar device. The longitudinal voltage V_{xx} is probed between the two bottom contacts. The scale bar represents $2\ \mu\text{m}$. The white, dashed rectangle marks the area where the voltage is probed. (c) Raman spectrum taken on the Hall bar at the position of the red star in panel (f). The prominent G and 2D peaks of Gr are seen at around $1580\ \text{cm}^{-1}$ and $2680\ \text{cm}^{-1}$, respectively. The Raman line at $1365\ \text{cm}^{-1}$ comes from the hBN substrate. (d) Raman spectra obtained on the uncovered substrate next to the Hall bar (black star in panel (f)) and on the Hall bar (red star in panel (f)). The characteristic silicon peaks have a higher amplitude on the uncovered wafer as compared to the hBN-Gr-hBN covered area. (e) SFM image of the Hall bar device. The scale bar represents $2\ \mu\text{m}$. (f) Scanning Raman microscopy image of the device. The intensity of the silicon peak at $520\ \text{cm}^{-1}$ is color encoded. (g) Line cut of the SFM image along the yellow, dashed line in panel (e). (h) Line cut of the scanning Raman microscopy image along the yellow, dashed line in panel (f) (black line). The red line represents the convolution of a step function with a Gaussian profile with a standard deviation of $250\ \text{nm}$ (green curve).

the doping profiles discussed below.

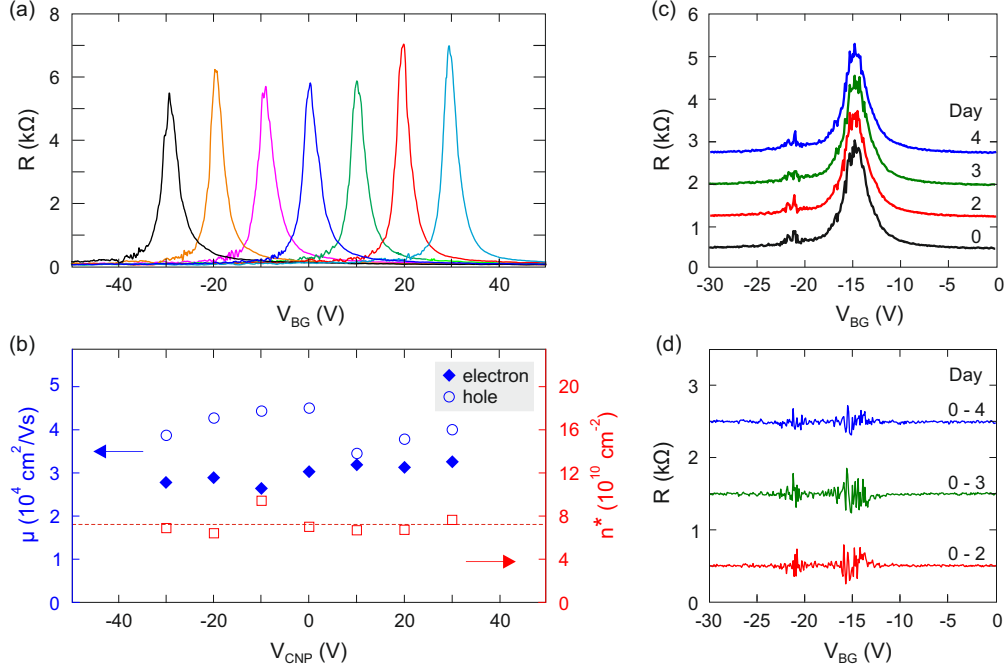


Figure 2: (a) Transport measurements highlighting the photo-induced doping effect. Seven back gate characteristics of the device with different CNPs ranging from -30 to 30 V. (b) Electron and hole mobilities (μ_e and μ_h) and charge carrier density fluctuations around the CNP (n^*) as extracted from the curves in panel (a). All three quantities remain mostly constant under application of the photo-induced doping effect. (c) Back gate characteristics of the device taken immediately after a doping profile was written and 2, 3, and 4 days later. The traces are offset for clarity by 750 Ω . (d) The traces from panel c recorded after 2, 3, and 4 days are subtracted from the curve measured immediately after the doping profile was written. The traces are offset by 1 k Ω each.

The combination of an electrically contacted device with a confocal laser setup allows us to investigate the spatial control of the laser-induced doping profiles in Gr-hBN heterostructures. Ju and coworkers¹⁸ attributed the photo-induced doping effect in hBN-Gr structures to nitrogen vacancies and carbon defects in the hBN, which give rise to defect states deep in the band gap with energies of 2.8 eV (nitrogen vacancy) and 2.6 eV (carbon impurity).²³ They argue that with the help of photons, these states can be occupied by charge carriers injected from the gated graphene.¹⁸ When the laser is turned on, charge carriers occupying defect states in the hBN layer are excited and, due to the applied gate voltage, move toward the graphene sheet, leaving behind oppositely charged states in the hBN layer. This process continues until the back gate is fully screened by the increasingly charged hBN layer (see also Figure 1a). When turning the laser off again, this

effect has effectively shifted the charge neutrality point (CNP) of the graphene sheet to the chosen value of the back gate voltage. Our laser energy of 2.33 eV in combination with the rather high laser intensity (2 to 4 mW) leads to high doping rates, such that only short illumination times are required to shift the CNP.

We expect that the strong photo-induced doping effect in hBN-Gr stacks on SiO₂ is closely related to the asymmetric gate oxide structure, i.e. the presence of the insulating SiO₂ layer underneath the hBN. The charges injected in the hBN likely diffuse to the bottom of the hBN layer in the direction of the electric field from the Si⁺⁺ back gate until they are stopped at the SiO₂/hBN interface. However, further investigations on the physical mechanisms of the photo-induced doping effect require different sample geometries and spectroscopy analysis techniques, which are beyond the scope of this manuscript. In this work, we focus on the creation, the erasing, the rewriting, and most importantly the spatial resolution of laser-induced doping profiles in this material stack, which do not rely on the use of photo-resists or masks.

In Figure 2a we show that this effect can be employed to shift the CNP to arbitrary negative as well as positive back gate voltages. To set the CNP of the entire graphene Hall bar to a specific value, we apply the corresponding back gate voltage and scan over the full area depicted in Figure 1f with a total illumination time of 120 s. The typical back gate characteristic of graphene²⁴ is maintained in all cases. From each back gate characteristic, we extract the electron mobility μ_e , the hole mobility μ_h , and the charge carrier density fluctuation n^* . The latter has been extracted by the method described in Reference 16 and is a good measure for the electronic disorder (i.e. electron-hole puddles) in bulk graphene. We find average values of $\mu_e = 30,000 \text{ cm}^2/(\text{Vs})$, $\mu_h = 40,000 \text{ cm}^2/(\text{Vs})$, and $n^* = 7 \times 10^{10} \text{ cm}^{-2}$ (see Figure 2b). Importantly, μ_e , μ_h , and n^* remain mostly constant for each chosen CNP, which shows the non-destructive nature of this process (Figure 2b). After turning the laser off, the back gate characteristic at 4.2 K remains unchanged for at least four days, which is the longest we have waited without manipulating the doping profile of the sample (see Figures 2c and d).

After demonstrating that we can shift the CNP of the entire Hall bar, we next focus on defining

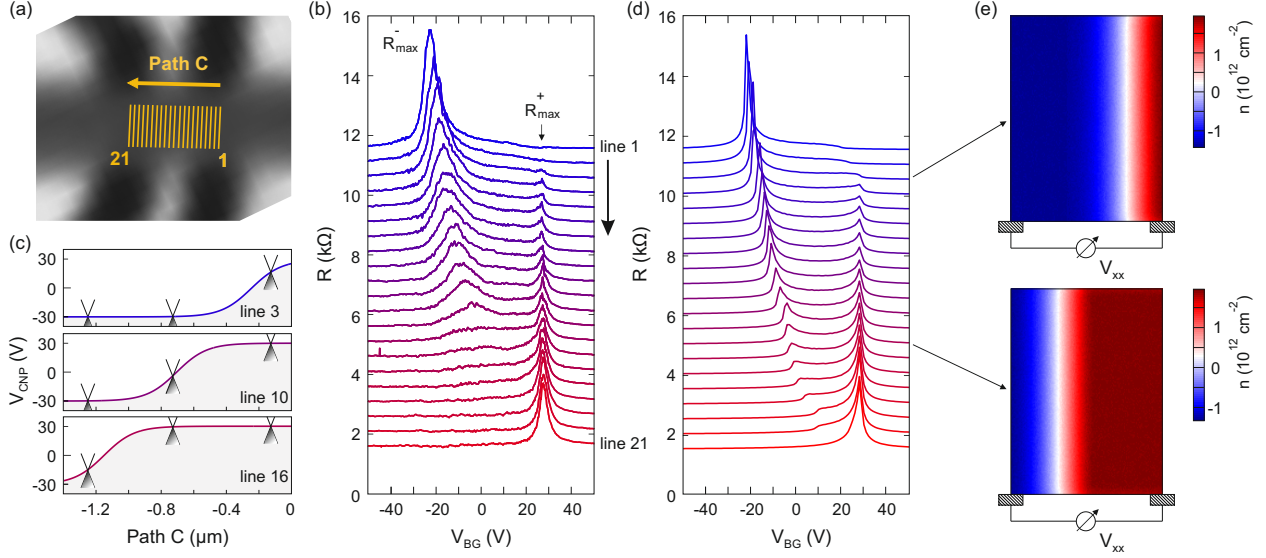


Figure 3: (a) Scanning, confocal Raman image of the integrated Si peak intensity. The orange lines indicate the parts written by the laser at a back gate voltage of +30 V to tune the area step by step from an n-doped regime via a local p-n junction to an entirely p-doped regime. (b) Back gate characteristics of the Hall bar measured after each individual line written with the laser (first back gate trace is at the top). The lines are offset for clarity by 500 Ω each (starting from line 21). (c) Illustration of the value of V_{CNP} along the horizontal extent of the sample for three different doping configurations. From top to bottom, the sample is increasingly more p-doped. (d) Simulated back gate traces. The parameters used are $\mu_e = 30,000 \text{ cm}^2/(\text{Vs})$, $\mu_h = 40,000 \text{ cm}^2/(\text{Vs})$, and $n^* = 7 \times 10^{10} \text{ cm}^{-2}$. The standard deviation of the Gaussian used for the doping profile is 300 nm. From top to bottom a greater part of the four-probe contact area is set to +30 V. The lines are offset for clarity. (e) Two exemplary doping profiles used in the simulation.

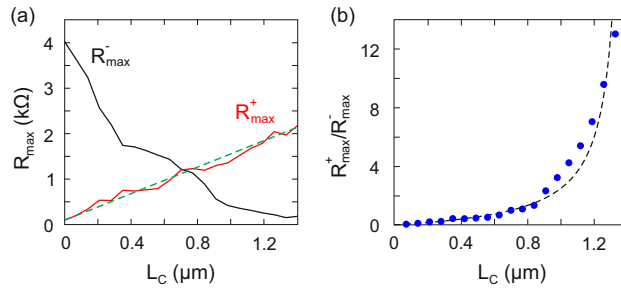


Figure 4: (a) The maximum resistance for the right (R_{max}^+ , red curve) and left (R_{max}^- , black curve) resistance peak of each trace shown in Figure 3b are extracted and plotted against the absolute value of the position of the last line written by the laser along "Path C" L_C indicated in Figure 3a. The green, dashed line is a linear fit with a slope of 1.4 Ω/nm highlighting the expected linear trend of R_{max}^+ considering simple, diffusive transport. (b) The ratio of the peak resistances shown in panel (a) ($R_{\text{max}}^+/R_{\text{max}}^-$) is plotted against L_C (blue points). The dashed, black line is given by the expression $L_C/(L_0 - L_C)$ with $L_0 = 1.4 \mu\text{m}$. It shows the behavior from assuming that the graphene sheet consists of two resistances in series, one for the n-doped and one for the p-doped regime.

spatially varying doping patterns within the graphene sheet. This aspect is highly interesting for potential applications as it enables the definition of re-writable, in-plane p-n and n-p-n junctions with any desired pattern, size, and orientation. To examine the spatial precision of our approach, we start by continuously moving the CNP in the sensitive four-probe area from -30 V to +30 V. In the beginning, the CNP of the entire sample is set to -30 V by scanning over the sample with our laser. Simultaneously, we record a Raman image of the prominent Si line. The integrated Si line intensity is displayed in Figure 3a. In the following, the laser is turned off and the back gate voltage is set to +30 V. Afterward, the laser is turned on for writing a single line across the Hall bar on the very right side of the four-probe area (see vertical line 1 in Figure 3a). The total illumination time during the writing of the line was 7 s. After switching the laser off again, the back gate characteristic of the device is probed, resulting in the upper curve in Figure 3b. This procedure is repeated 20 times. In every iteration, the written line is intentionally shifted by ~ 70 nm to the left (vertical arrow and “Path C” in Figure 3a). The resistance curves obtained after each iteration are displayed in Figure 3b, with the lines offset for clarity. With each line, the CNP of a greater part of the sensitive area is set to +30 V, resulting in the appearance of a typical graphene p-n junction back gate characteristic²⁵ (middle part of Figure 3b). Additionally, stray light from the laser leads to a continuous doping of the Hall bar and as a result the initial Dirac peak is gradually broadened and shifted toward positive voltages. This effect is especially strong after writing the first line, when the initial Dirac peak is not anymore at -30 V but is shifted to -23 V. Finally, after the entire four-probe area was covered with lines written by the laser, the initial, left Dirac peak has completely vanished and only the new CNP at +30 V can be seen in the back gate characteristic (line 21 in Figure 3b). The steady and continuous shift from an entirely electron-doped four-probe area over a p-n junction to an entirely hole-doped area (see evolution from top to bottom panel in Figure 3c) demonstrates the high spatial precision with which doping profiles can be made with this technique.

To cross-check the measurements, we employ a simple, purely diffusive charge transport model, in which we divide the area where V_{xx} is probed ($1.4 \mu\text{m} \times 1.9 \mu\text{m}$; compare white, dashed rect-

angle in Figure 1b) into individual squares with a size of $10 \text{ nm} \times 10 \text{ nm}$ each. To each square we then assign a charge distribution

$$n_{ij}(V_{\text{BG}}) = n_{\text{dop},ij} + n_{\text{gate}}(V_{\text{BG}}) + n_{ij}^*, \quad (1)$$

consisting of three contributions. The first contribution, $n_{\text{dop},ij}$, is the spatially varying doping profile due to the photo-induced doping effect. Each written laser line is modeled as a Gaussian with a standard deviation of 300 nm, which slightly differs from the experimentally determined value (250 nm, see Figure 1h) to account for various experimental uncertainties as described below. Additionally, we add a constant offset to incorporate the initial homogeneous photo-induced doping of the sample. We adjust this constant offset for each trace to account for the increasing stray light-induced doping of the sample. The second contribution, $n_{\text{gate}}(V_{\text{BG}}) = \alpha V_{\text{BG}}$, accounts for the field-effect-induced charge carrier density during a back gate sweep, with $\alpha = 5.5 \times 10^{10} \text{ V}^{-1} \text{ cm}^{-2}$ being the capacitive coupling constant of the back gate as extracted from quantum Hall measurements (not shown). The final contribution, n_{ij}^* , represents the built-in charge density variations across the sample. In our model, we implement it by assigning a randomly generated number uniformly distributed between $-n^*/2$ and $n^*/2$ to each square. Finally, we compute the conductivity of every square by

$$\sigma_{ij} = e\mu|n_{ij}| + \sigma_0, \quad (2)$$

where e is the elementary charge, n_{ij} the charge carrier density of the square and σ_0 is a residual conductivity to account for the finite resistance of graphene at the charge neutrality point adjusted to 10^{-4} S to reproduce the data. Furthermore, μ is the electron/hole mobility, depending on the sign of n_{ij} , for which we use the average values of $\mu_e = 30,000 \text{ cm}^2/(\text{Vs})$ and $\mu_h = 40,000 \text{ cm}^2/(\text{Vs})$, as obtained from the six back gate traces in Figure 2a. By applying Ohm's law to each square and relating the currents and voltages of each square via Kirchhoff's laws, we calculate the total resistance of the graphene sheet from the applied bias voltage and the total outgoing current.

We end up with the simulated back gate characteristics shown in Figure 3d, which match the experimental results quite well. In Figure 3e the corresponding doping profiles of $n_{\text{dop},ij}$ across the four-probe area for two exemplary back gate traces are visualized. The fact that our simple model is able to reproduce the most prominent features of our measurements clearly indicates that the photo-induced doping effect can indeed be effectively used to define spatially resolved doping patterns.

In Figure 4a, we show the maximum resistance value measured at around +30 V back gate voltage R_{max}^+ (red trace) as well as the maximum value obtained for negative back gate voltage R_{max}^- (black trace) as highlighted in Figure 3b. Both peak resistances are plotted against L_C , which is defined as the absolute value of the position of the last, exposed line along "Path C" prior to measuring the corresponding back gate trace. We observe that with increasing L_C , R_{max}^+ increases linearly, while R_{max}^- drops. In particular, the linear increase of R_{max}^+ is in good agreement with simple, diffusive transport considerations, where R_{max}^+ is completely dominated by the length of the sample area with a Dirac point at +30 V. This area increases linearly with L_C , explaining the dependence of $R_{\text{max}}^+ \propto L_C$. From a linear fit to the data (see green, dashed line in Figure 4a) we extract a resistance change per length of $\Delta R_{\text{max}}^+ / \Delta L_C = 1.4 \text{ } \Omega/\text{nm}$. In Figure 4b the ratio of both resistance peaks $R_{\text{max}}^+ / R_{\text{max}}^-$ is shown (blue points). The continuous increase can be understood from simple diffusive transport considerations. In this case, the ratio of the resistance peaks is given by $R_{\text{max}}^+ / R_{\text{max}}^- = L_C / (L_0 - L_C)$, where $L_0 = 1.4 \text{ } \mu\text{m}$. This value highlights the very high sensitivity in resistance change as function of exposed area (i.e. length), which might be of interest for future applications. This expression describes the resistance ratio without any free parameters. The corresponding curve is shown in Figure 4b (dashed, black line). It shows excellent agreement with our measurements. From this representation it is evident that we continuously change the doping profile along "Path C" upon writing individual lines with a step width of $\sim 70 \text{ nm}$ and very high spatial precision. Our results show that the resolution of this technique is essentially only limited by the size of the laser spot and the accuracy of sample positioning.

The high spatial precision of the laser-induced doping technique allows the writing and erasing

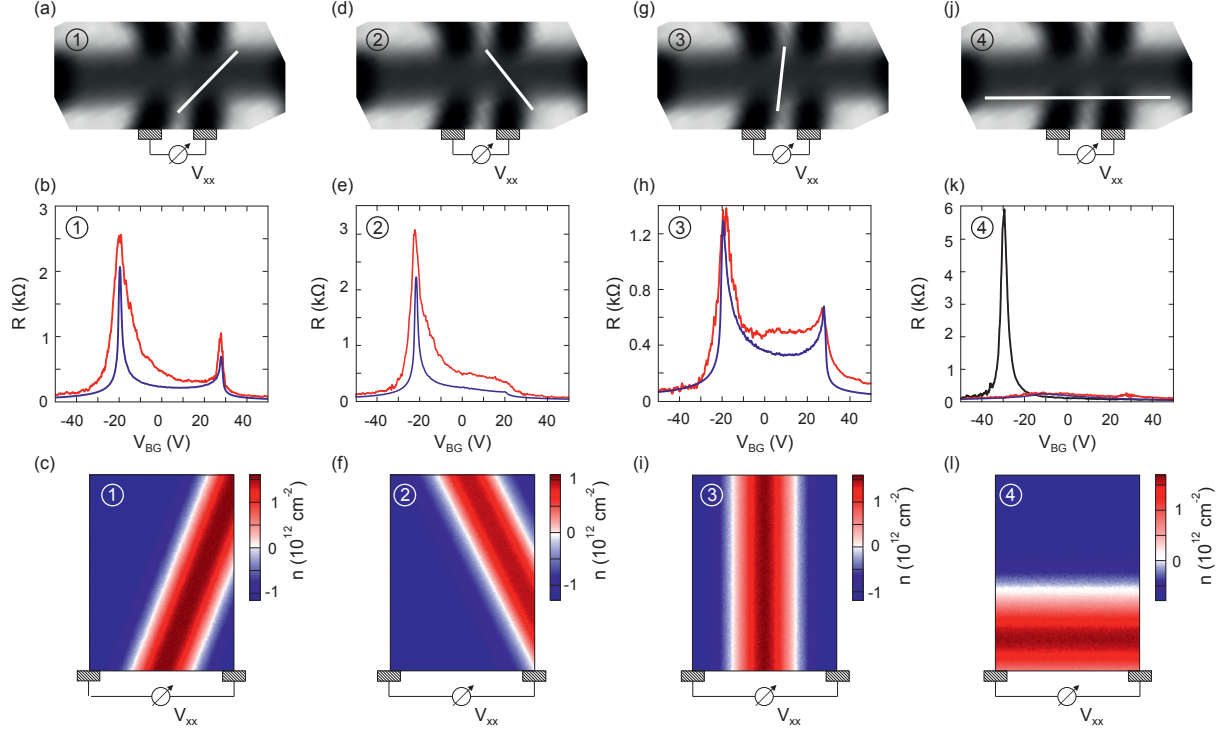


Figure 5: (a) Scanning Raman image of the integrated Si peak intensity. The line indicates the doping pattern that was written with the laser. (b) The measured (red) and simulated (blue) back gate characteristics after writing line 1 (see panel (a)). The initial CNP, which was set to -30 V, is shifted to more positive values due to stray light from the laser when writing the line at +30 V. (c) Doping profile of line 1 (compare panel (a)) as used in the model trace shown in panel (b). The standard deviation of the Gaussian doping profile was set to 200 nm. (d,e,f) The same as panels (a,b,c) where line 2 (see panel (d)) was written with the laser after resetting the entire device to a CNP of -30 V (see main text). The standard deviation of the Gaussian doping profile (see panel (f)) used in the model was also set to 200 nm. (g,h,i) The same as panels (a,b,c) where line 3 (see panel (g)) was written with the laser after resetting the entire device to a CNP of -30 V (see main text). The standard deviation of the Gaussian doping profile (see panel (i)) used in the model was set here to 230 nm. (j,k,l) The same as panels (a,b,c) where line 4 (see panel (j)) was written with the laser after resetting the entire device to a CNP of -30 V (see main text). The black line in panel (k) represents the measured back gate characteristic prior to writing line 4, when the entire sample was still set to $V_{\text{CNP}} = -30$ V. In this case, the standard deviation of the Gaussian doping profile (see panel (l)) used in the model was set to 330 nm.

of distinct, well-defined doping profiles. We demonstrate this by writing four different lines with the laser as illustrated in Figures 5a, 5d, 5g, and 5j. In all four cases, the entire sample was first set to a CNP of -30 V before the individual lines were written at a back gate voltage of +30 V. For each case, we cross-check the measurements by using the simple diffusive model described above (and used in Figure 3d) to simulate a similar doping geometry. As before, we adapt the constant doping offset in the simulation to account for stray light from the written lines at +30 V that slightly shifts the -30 V CNP in the rest of the device. We also adjust the width of the simulated Gaussian profile to compensate for uncertainties during the measurement such as a possible misalignment of the optical path and positioning uncertainties due to creeping effects of the piezo stage. Adjusting the width of the Gaussian also partly compensates for the fact that the actual shape of the doping profile induced by a single laser line is not exactly a Gaussian. Once enough charge carriers in the hBN have been excited so that the hBN layer completely screens away the back gate-induced electric field, the photo-doping effect stops and hence the actual doping profile most likely has a saturation area in the center, where the intensity is highest. A good Gaussian profile might only be obtained by perfectly adjusting illumination time and laser intensity to one another.

We start by writing line 1 (see Figure 5a), introducing a p-n junction between the two contacts where V_{xx} is probed. The resulting back gate characteristic is shown in red in Figure 5b, showing the typical p-n junction behavior with two resistance peaks at -20 V and +30 V. It is again evident that stray light plays an important role, as the initial, left CNP is shifted from the original -30 V to -20 V and is also more smeared out than the newly written CNP at positive gate voltage. To confirm the p-n junction doping profile, we calculate the back gate characteristic of a comparable doping pattern (shown in Figure 5c). The resulting trace (blue curve in Figure 5b) reproduces the main features of the measured trace quite well. After erasing the written doping profile and resetting the CNP of the entire Hall bar to -30 V, line 2 is written, again at a back gate voltage of +30 V. As seen in Figure 5d, there is now a conducting path connecting the relevant contacts that is not crossed by the laser line and consequently has its expected CNP at the original -30 V. The measured trace (red line in Figure 5e) indeed shows only one distinct peak at negative gate voltage. This is further

backed up by the simulated trace (blue trace in Figure 5e) using the doping profile depicted in Figure 5f. After resetting the CNP of the Hall bar to -30 V, line 3 is written. The measured back gate trace (see red line in Figure 5h) shows two peaks at -20 V and +30 V. Compared to line 1, the peak resistance is significantly lower and the right peak is less distinct, which can be attributed to the above mentioned experimental uncertainties. This is further supported by the calculation (see blue line in Figure 5h), for which the width of the Gaussian profile had to be slightly increased (see Figure 5i). However, from the measurements it is evident that an n-p-n junction can be accurately written with this technique on a length as low as 1.4 μm . Finally, we investigate a fourth interesting doping profile. Again, we first set the entire Hall bar to a CNP of -30 V. The resulting back gate characteristic with a single Dirac peak at -30 V can be seen in Figure 5k (black trace). Afterward, line 4 is written with the laser at +30 V. Since the laser line runs in parallel to the path along which V_{xx} is probed, there is now a highly doped path from source to drain for every value of the back gate voltage, which is reflected in the measured back gate trace, shown in Figure 5k (red curve). As expected, the resistance over the whole range of the back gate voltage is much lower than the resistance measured at the CNP in the homogeneously doped case (black trace). This is further supported by the calculated back gate trace (blue line in Figure 5k) using the doping profile shown in Figure 5l. In all four cases, the qualitative match between the measured and simulated traces indicates that the written laser lines indeed produce the desired doping geometries.

In conclusion, we demonstrated that controllable, laser-induced doping in graphene-hBN heterostructures can be used to define long-term stable doping patterns such as p-n and n-p-n junctions with high spatial resolution and without the use of masks and photo-resists. The CNP of the device can be shifted to any desired value of the back gate voltage without reducing the charge carrier mobility. We focused on the spatial resolution of this technique and demonstrated the continuous evolution of an entirely n-doped graphene regime via a local p-n junction to a fully p-doped regime by step-by-step illumination of small areas of the graphene Hall bar with a green laser. Cross-checking the data with a simple, fully diffusive transport model further underlines that our technique is in principle only limited by the laser spot size (Gaussian standard deviation of 250 nm) and the ac-

curacy of the piezo stage, making it comparable to conventional optical lithography techniques. Consequently, we wrote and erased different doping pattern geometries in a single Hall bar device, creating e.g. a custom-made n-p-n junction. This optical approach to locally dope high-quality graphene devices has distinct advantages over conventional techniques that make use of local gate electrodes in terms of rewritability and a reduction of the amount of difficult and possibly invasive lithography, etching, and contacting steps.^{9,10} Additionally, doping patterns with numerous p-n junctions could be implemented and erased in a single device, opening unprecedented opportunities to study graphene-based electron optic devices,^{26–28} Veselago lenses,²⁹ and Klein tunneling phenomena.³⁰ Moreover, other complex doping profiles which are difficult or impossible to realize with conventional gate electrodes, like isolated, localized doping spots and arrays, can be realized with this technique. Likely, the photo-induced doping effect can be extended to other van der Waals heterostructures based on hBN, opening a wide range of possible studies on the creation of lateral transition-metal-dichalcogenide-hBN transistors without local gate electrodes.

Acknowledgement

The authors thank M. Drögeler and F. Hassler for helpful discussions. Support by the Helmholtz Nanoelectronic Facility (HNF), the Deutsche Forschungsgemeinschaft, the ERC (GA-Nr. 280140), and the EU project Graphene Flagship (contract no. NECT-ICT-604391), are gratefully acknowledged. S. R. acknowledges funding by the National Research Fund (FNR) Luxembourg.

References

- (1) Ponomarenko, L. et al. *Nature* **2013**, 497, 594–597.
- (2) Dean, C.; Wang, L.; Maher, P.; Forsythe, C.; Ghahari, F.; Gao, Y.; Katoch, J.; Ishigami, M.; Moon, P.; Koshino, M.; Taniguchi, T.; Watanabe, K.; Shepard, K.; Hone, J.; Kim, P. *Nature* **2013**, 497, 598–602.
- (3) Hunt, B.; Sanchez-Yamagishi, J.; Young, A.; Yankowitz, M.; LeRoy, B. J.; Watanabe, K.;

- Taniguchi, T.; Moon, P.; Koshino, M.; Jarillo-Herrero, P.; Ashoori, R. *Science* **2013**, *340*, 1427–1430.
- (4) Woods, C. et al. *Nature Physics* **2014**, *10*, 451–456.
- (5) Britnell, L.; Ribeiro, R.; Eckmann, A.; Jalil, R.; Belle, B.; Mishchenko, A.; Kim, Y.-J.; Gorbachev, R.; Georgiou, T.; Morozov, S.; Grigorenko, A.; Geim, A.; Casiraghi, C.; Castro Neto, A.; Novoselov, K. *Science* **2013**, *340*, 1311–1314.
- (6) Withers, F.; Del Pozo-Zamudio, O.; Mishchenko, A.; Rooney, A.; Gholinia, A.; Watanabe, K.; Taniguchi, T.; Haigh, S.; Geim, A.; Tartakovskii, A.; Novoselov, K. *Nature Materials* **2015**, *14*, 301–306.
- (7) Lu, C.-P.; Li, G.; Watanabe, K.; Taniguchi, T.; Andrei, E. Y. *Physical Review Letters* **2014**, *113*, 156804.
- (8) Decker, R.; Wang, Y.; Brar, V. W.; Regan, W.; Tsai, H.-Z.; Wu, Q.; Gannett, W.; Zettl, A.; Crommie, M. F. *Nano Letters* **2011**, *11*, 2291–2295.
- (9) Wang, L.; Meric, I.; Huang, P.; Gao, Q.; Gao, Y.; Tran, H.; Taniguchi, T.; Watanabe, K.; Campos, L.; Muller, D.; Guo, J.; Kim, P.; Hone, J.; Shepard, K.; Dean, C. *Science* **2013**, *342*, 614–617.
- (10) Engels, S.; Terrés, B.; Klein, F.; Reichardt, S.; Goldsche, M.; Kuhlen, S.; Watanabe, K.; Taniguchi, T.; Stampfer, C. *Physica Status Solidi (b)* **2014**, *251*, 2545–2550.
- (11) Engels, S.; Terrés, B.; Epping, A.; Khodkov, T.; Watanabe, K.; Taniguchi, T.; Beschoten, B.; Stampfer, C. *Physical Review Letters* **2014**, *113*, 126801.
- (12) Neumann, C.; Reichardt, S.; Drögeler, M.; Terrés, B.; Watanabe, K.; Taniguchi, T.; Beschoten, B.; Rotkin, S. V.; Stampfer, C. *Nano Letters* **2015**, *15*, 1547–1552.
- (13) Kretinin, A. et al. *Nano Letters* **2014**, *14*, 3270–3276.

- (14) Dean, C.; Young, A.; Meric, I.; Lee, C.; Wang, L.; Sorgenfrei, S.; Watanabe, K.; Taniguchi, T.; Kim, P.; Shepard, K.; Hone, J. *Nature Nanotechnology* **2010**, *5*, 722–726.
- (15) Britnell, L.; Gorbachev, R.; Jalil, R.; Belle, B.; Schedin, F.; Mishchenko, A.; Georgiou, T.; Katsnelson, M.; Eaves, L.; Morozov, S.; Peres, N.; Leist, J.; Geim, A.; Novoselov, K.; Ponomarenko, L. *Science* **2012**, *335*, 947–950.
- (16) Couto, N. J.; Costanzo, D.; Engels, S.; Ki, D.-K.; Watanabe, K.; Taniguchi, T.; Stampfer, C.; Guinea, F.; Morpurgo, A. F. *Physical Review X* **2014**, *4*, 041019.
- (17) Drögeler, M.; Volmer, F.; Wolter, M.; Terrés, B.; Watanabe, K.; Taniguchi, T.; Güntherodt, G.; Stampfer, C.; Beschoten, B. *Nano Letters* **2014**, *14*, 6050–6055.
- (18) Ju, L.; Velasco Jr, J.; Huang, E.; Kahn, S.; Nosiglia, C.; Tsai, H.-Z.; Yang, W.; Taniguchi, T.; Watanabe, K.; Zhang, Y.; Zhang, G.; Crommie, G.; Zettl, A.; Wang, F. *Nature Nanotechnology* **2014**, *9*, 348–352.
- (19) Kim, Y. D.; Bae, M.-H.; Seo, J.-T.; Kim, Y. S.; Kim, H.; Lee, J. H.; Ahn, J. R.; Lee, S. W.; Chun, S.-H.; Park, Y. D. *ACS Nano* **2013**, *7*, 5850–5857.
- (20) Tiberj, A.; Rubio-Roy, M.; Paillet, M.; Huntzinger, J.-R.; Landois, P.; Mikolasek, M.; Contreras, S.; Sauvajol, J.-L.; Dujardin, E.; Zahab, A.-A. *Scientific Reports* **2013**, *3*, 2355.
- (21) Banszerus, L.; Schmitz, M.; Engels, S.; Dauber, J.; Oellers, M.; Haupt, F.; Watanabe, K.; Taniguchi, T.; Beschoten, B.; Stampfer, C. *Science Advances* **2015**, *1*, e1500222.
- (22) Neumann, C.; Reichardt, S.; Venezuela, P.; Drögeler, M.; Banszerus, L.; Schmitz, M.; Watanabe, K.; Taniguchi, T.; Mauri, F.; Beschoten, B.; Rotkin, S. V.; Stampfer, C. *Nature Communications* **2015**, *6*, 8429.
- (23) Attacalite, C.; Bockstedte, M.; Marini, A.; Rubio, A.; Wirtz, L. *Physical Review B* **2011**, *83*, 144115.

- (24) Novoselov, K. S.; Geim, A. K.; Morozov, S.; Jiang, D.; Zhang, Y.; Dubonos, S.; Grigorieva, I.; Firsov, A. *Science* **2004**, *306*, 666–669.
- (25) Williams, J.; DiCarlo, L.; Marcus, C. *Science* **2007**, *317*, 638–641.
- (26) Rickhaus, P.; Maurand, R.; Liu, M.-H.; Weiss, M.; Richter, K.; Schönenberger, C. *Nature Communications* **2013**, *4*, 2342.
- (27) Young, A. F.; Kim, P. *Nature Physics* **2009**, *5*, 222–226.
- (28) Taychatanapat, T.; Tan, J. Y.; Yeo, Y.; Watanabe, K.; Taniguchi, T.; Özyilmaz, B. *Nature Communications* **2015**, *6*, 6093.
- (29) Cheianov, V. V.; Fal’ko, V.; Altshuler, B. *Science* **2007**, *315*, 1252–1255.
- (30) Beenakker, C. *Reviews of Modern Physics* **2008**, *80*, 1337.

Graphical TOC Entry

